Journal of Nuclear Medicine, published on July 14, 2016 as doi:10.2967/jnumed.116.176784

Tumor uptake of anti-CD20 Fabs depends on tumor perfusion

Claudia Theresa Mendler[1,2*#], Annette Feuchtinger[3*], Irina Heid[4*], Michaela Aichler[3], Calogero D'Alessandria[1], Sabine Pirsig[1], Birgit Blechert[1], Hans-Jürgen Wester[5], Rickmer Braren[4], Axel Walch[3], Arne Skerra[2], Markus Schwaiger[1#]

[1]Nuklearmedizinische Klinik und Poliklinik, Klinikum rechts der Isar, Technische Universität München, D-81675 München, Germany

[2]Munich Center for Integrated Protein Science (CIPS-M) and Lehrstuhl für Biologische Chemie, Technische Universität München, D-85354 Freising (Weihenstephan), Germany

[3]Research Unit Analytical Pathology – Institute of Pathology, Helmholtz Zentrum München, D-85764 Neuherberg, Germany

[4]Department of Radiology, Klinikum rechts der Isar, Technische Universität München, D-81675 München, Germany

[5]Pharmaceutical Radiochemistry, Technische Universität München, D-85748 Garching, Germany

*contributed equally to this work

[#]correspondence to Prof. Dr. Markus Schwaiger or Claudia Mendler

Nuklearmedizinische Klinik und Poliklinik, Klinikum rechts der Isar der Technischen Universität München, Ismaninger Straße 22, D-81675 München, Germany; phone: +49 89 4140 2972; fax: +49 89 4140 4841; e-mail: Markus.Schwaiger@tum.de, claudia.mendler@wzw.tum.de

Running title: Perfusion study of lymphoma xenografts

Key words: 3D light-sheet fluorescence microscopy, DCE-MRI, Fab fragment, lymphoma, tumor perfusion

Financial support:

This study was supported by ERC Grant MUMI, ERC-2011-ADG_20110310 and by the Deutsche Forschungsgemeinschaft, Collaborative Research Centre SFB 824.

Disclosure:

No potential conflicts of interest were disclosed.

Word count:

Text: 5596 words

Total number of figures and tables:

5 Figures

ABSTRACT

Antibodies have become an established treatment modality in cancer therapy during the last decade. However, these treatments often suffer from insufficient and heterogeneous response despite validated antigen or target receptor expression in the tumor. In fact, therapeutic success depends on both the presence and accessibility of the tumor antigen by the antibody. In search of a suitable preclinical animal model to evaluate the mechanisms of tumor heterogeneity and hemodynamics, we characterized two exemplary non-Hodgkin lymphoma subtypes with comparable CD20 expression and metabolism, SUDHL-4 and Granta, using multimodal imaging techniques. **Methods:** To investigate *in vivo* biodistribution, two differently modified αCD20 antigen-binding fragments (Fab), prepared (i) by PASylation and (ii) by fusion with an albumin-binding domain, were radiolabeled with ^{125}I and intravenously injected into immunocompromised mice bearing corresponding xenografts. **Results:** Validation with ^{18}F-FDG revealed similar distribution of vital tumor tissue 1 h p.i. However, large differences in tumor uptake were observed when applying the CD20-specific radiotracers ^{125}I-Fab-ABD and ^{125}I-Fab-PAS$_{200}$ with 12.3 and 2.4 % ID/g, respectively, for Granta in comparison with 3.5 and 0.75 % ID/g, respectively, for SUDHL-4 xenografts 24 h p.i. 3D light-sheet fluorescence microscopy with Cy5-Fab-PAS$_{200}$ confirmed better tracer extravasation in the Granta tumors. Moreover, dynamic contrast enhanced MRI imaging revealed significantly reduced tumor perfusion in the SUHDL-4 xenografts. **Conclusion:** Tracer uptake was highly dependent on local tumor perfusion as well as Fab permeation in the SUDHL-4 and Granta tumors. Thus, the SUDHL-4 xenograft offers an excellent model system to investigate the influence of therapies affecting tumor angiogenesis.

INTRODUCTION

Non-Hodgkin lymphomas (NHL) are among of the most common malignancies accounting for approximately 4 % of all cancers. Most of them originate from B-cells, which express the integral transmembrane protein CD20 at high levels. NHL subtypes are characterized by a distinct histopathologic anatomy and a complex and variable vascularity (*1*).

Antibody-based therapy, including radioimmunotherapy, is one of the most important strategies for treating patients with lymphomas as well as solid tumors today (*2*). Recently, tumor accumulation and heterogeneity of ^{111}In-Ibritumomab tiuxetan as well as ^{18}F-FDG was analyzed and compared to the radioimmunotherapy response in 16 patients with B-cell NHL (*3*). It was found that the heterogeneity of intratumoral ^{111}In-Ibritumomab tiuxetan distribution, rather than the absolute level of antibody uptake, correlated with tumor response. Interestingly, no differences in heterogeneity were observed between responder and non-responder groups when using the small molecule metabolic radiotracer ^{18}F-FDG.

Such studies clearly show that therapeutic success is highly influenced by the intratumoral access of the therapeutic antibody reagent, a generally problematic feature of this class of high molecular weight proteins. Especially in radioimmunotherapy a non-uniform distribution within tumors appears to limit efficacy (*4*). Therefore, attempts are made for searching diagnostic biomarkers to predict therapeutic outcome by using histopathology (*5*) or perfusion measurements (*1*).

To our knowledge there are no well characterized preclinical xenograft models showing mutually similar tumor biology and target expression in spite of profound differences in tumor perfusion. Hence, the goal of this study was to compare and investigate two exemplary NHL subtypes, the mantle cell lymphoma cell line Granta519 (*6*) and the diffuse large B-cell lymphoma cell line SUDHL-4 (*7*), which exhibit similar CD20 expression level, as subcutaneous human tumor xenograft models in immunocompromised mice using multimodal imaging methods.

MATERIALS AND METHODS

Preparation and radioiodination of αCD20 Fabs

The CD20-specific Fab, derived from Ofatumumab, was produced in *E. coli* in two versions, either fused with an albumin-binding domain (ABD) or with a long conformationally disordered amino acid sequence consisting of proline, alanine and serine (PAS) and labeled with ^{125}I using the Iodogen method as previously described (*8*).

Radiosynthesis of ^{18}F-FDG

^{18}F-FDG was produced by the Radiopharmacy Unit, Technische Universität München, essentially as described before (*9*).

In vivo studies

SUDHL-4 and Granta cells were grown in RPMI medium supplemented with 10 % (v/v) fetal bovine serum and 1 mM L-glutamine. CB-17 SCID mice (Charles River Laboratories) were injected subcutaneously with 10 x 10^6 SUDHL-4 or 5 x 10^6 Granta cells suspended in 100 µl of a 50 % (v/v) mixture of RPMI medium and Matrigel (Sigma-Aldrich). A maximum size of approximately 800 mm^3 was used for all experiments. For biodistribution studies, mice (n=5) were injected intravenously with 0.5 MBq of ^{125}I-Fab-PAS$_{200}$ or ^{125}I-Fab-ABD as described before (*8*). All animal experiments were in compliance with regulatory and institution guidelines and approved by the local authorities (Regierung von Oberbayern, Germany; licence 55.2-1-54-2532-87-11).

Histology and Immunohistochemistry

Excised specimen were fixed in 4 % (w/v) neutrally buffered formalin, embedded in paraffin and cut into 3 µm slices. Immunohistochemical staining was performed on a Discovery XT automated stainer (Ventana) using the following antibodies: MIB1 (DCS Innovative Diagnostik-Systeme); CD31 (Abcam); CD20 (DakoCytomation); Caspase 3 (Cell Signaling); with Discovery Universal (Ventana) as secondary

antibody. Signal detection was performed using the peroxidase/diaminobenzidine reaction (Roche, Ventana). Quantification of immunohistological staining was performed by image analysis using Developer XD2 software (Definiens) following a previously published procedure (*10*).

Autoradiography

Tumor sections (10 µm) were incubated for 2 h (^{18}F) or 12 h (^{125}I) on the Kodak Storage Phosphor screen GP (Eastman Kodak Company) in the dark. Distribution of radioactivity was subsequently quantified using a CR 35 BIO image plate scanner (Raytest Isotopenmeßgeräte) with an internal resolution of 25 µm, followed by image analysis with AIDA software (Raytest Isotopenmeßgeräte).

Light-Sheet Fluorescence microscopy (LSFM)

Fab-PAS_{200} (2 mg/ml) was coupled at 5:1 molar ration with Cy5-NHS ester (Lumiprobe) in 0.1 M $NaHCO_3$ pH 8.5 for 2 h at room temperature. After removal of excess dye via PD-10 column in phosphate buffered saline, a labeling ratio of 1.6 fluorophores per Fab was determined via UV-VIS spectroscopy.

CB-17 SCID mice were intravenously injected with 0.7 nmol Cy5-labeled Fab-PAS_{200} and, after 24 h, with 2 nmol Lectin from Bandeiraea (Griffonia) simplicifolia-Isolectin I (Sigma-Aldrich: L2380) labeled with VivoTag-S 750 (PerkinElmer) – for specific vessel visualization – followed by incubation for 5 min before the animals were sacrificed. Explanted xenografts were fixed in PaxGene (PreAnalytiX) as described (*11*) and then subjected to a chemical procedure of optical clearing (*12*).

Whole xenografts were imaged with a LaVision 3D ultramicroscope system (LaVision BioTec). The specimens were two-sided illuminated by a planar light-sheet using a white light laser (SuperK EXTREME EXW-9; NKT Photonics). Lectin and Cy5-Fab-PAS_{200} were excited at 740/35 nm and 640/30 nm, respectively, while the emitting light was detected using 795/50 nm and 690/50 filters. Optical sections were recorded by moving the specimen chamber vertically (step size = 5µm) through the laser light-

sheet. 3D-reconstructions were obtained using ImspectorPro 5.0.1 Software (LaVision BioTec) and arivis Vision4D (arivis).

DCE-MRI Experiments

Mice were anesthetized and placed in prone position on top of a 47 mm microscopy surface coil in the 1.5 T Achieva clinical scanner (Philips Medical Systems). An axial multi-slice T2-weighted turbo spin-echo sequence (resolution 0.3 x 0.3 x 0.7 mm^3, TE = 90 ms, TR > 3 s, NSA = 8) covering the complete tumor was applied as anatomical reference. DCE-MRI experiments were performed using a previously described fast single-shot Look-Locker based radial T1 mapping technique with the golden cut principle (*13,14*). One bolus dose of 0.04 mmol/kg of Gd-DTPA (Magnevist) was administered after 57 s of baseline measurement. Dynamic T1 mapping of one axial slice positioned over the tumor and spinal muscles was performed every 5.7 s for a total of 1075 s (resolution = 0.7 x 0.7 x 2 mm^3, TR/TE = 12.6/5.7 ms, radial profiles = 105, flip angle = 10°, T_{acq} = 2.6 s, T_{pause} = 3.1 s). DCE-MRI data were analyzed using in-house software. Areas under the Gd-concentration curve for vital tumor and spinal muscle were computed using Prism 5 (GraphPad).

Immunofluorescence

CB-17 SCID mice were injected i.v. with 15 mg/kg of Hoechst33342 (Sigma Aldrich) 1 min before sacrification. Tumor cryosections were stained with primary CD20-specific mouse clonal antibody (DakoCytomation) and CD31-specific rabbit polyclonal antibody (Abcam) using fluorescein-labeled goat anti-rabbit or Cy3-labeled goat anti-mouse IgG (both Invitrogen) as secondary antibodies. Fluorescence images were captured using an Axio Imager Z1 upright microscope system. Cy3-based signals were detected with a 43 HE DsRed filter set (Carl Zeiss), fluorescein based signals with a 38 HE Green Fluorescent Protein filter set (Carl Zeiss) and Hoechst33342 (H33342) dye with a 49 DAPI filter set (Carl Zeiss).

Diffusion analysis with H33342

Perfusion study of lymphoma xenografts

Images of the entire tumor sections were acquired at 200-fold magnification with an AxioImager Z1 (Zeiss) using the mosaic picture mode. For quantitative image analysis regions of interest (vital tumor) were identified and analysed using the Definiens Developer XD2 software (Definiens) as described (*15*). First, a specific rule set was defined to detect the CD31-stained vessel wall based on fluorescence-layer, intensity, shape and neighbourhood. Next, a distance map algorithm was applied to define distance ranges surrounding the vessels with stepwise increasing distance from 0–25 µm up to 175–200 µm. Finally, the overall mean H33342 intensity was calculated for each vessels and distance range.

Statistics

For comparison between two groups, Student's t test for unpaired data was used. P values of <0.05 were considered statistically significant.

RESULTS

Characterization of SUDHL-4 and Granta lymphoma xenografts

The xenograft tumor morphologies of the two distinct NHL cell lines Granta519 and SUDHL-4 were investigated with regard to *in vivo* biodistribution and autoradiography in immunocompromised mice using the metabolic radiolabel ^{18}F-FDG as well as the radioiodinated αCD20 tracers ^{125}I-Fab-PAS$_{200}$ and ^{125}I-Fab-ABD. ^{18}F-FDG autoradiography revealed a homogeneous distribution pattern in both xenografts, thus verifying metabolic activity and tumor viability (Fig. 1A). Also, the two versions of the CD20-specific Fab, both engineered for extended plasma half-life using either PASylation technology or an ABD, showed strong, though heterogeneous distribution in Granta tumors 24 h p.i. (Fig. 1A). In contrast, the SUDHL-4 xenograft exhibited an unusual rim of concentrated tracer signal with minimal radioactivity in the tumor lumen.

Perfusion study of lymphoma xenografts

These findings were confirmed by biodistribution experiments, which indicated strong tumor accumulation 24 h p.i. of 12.3 %ID/g and 2.4 %ID/g, respectively, for Fab-ABD and Fab-PAS_{200} as well as high tumor-to-organ ratios in the Granta xenografts (Supplemental Table 1). However, drastically reduced tumor uptake, by 3.5- and 3.2-fold for Fab-ABD and Fab-PAS_{200}, respectively, was observed for the SUDHL-4 tumors as also indicated by low tumor-to-organ ratios (Figs. 1B and 1C). Nevertheless, similar tracer distribution in the organs was found for both models. In addition, no correlation between tracer uptake and tumor size, typically in the range of 100-800 mm^2, was seen (Fig. 1D).

For efficient tumor uptake and tracer distribution, the expression pattern of the target antigen CD20 is crucial. In agreement with previously published data, high CD20 expression of both lymphoma cell lines was verified using FACS analysis of the cell lines (data not shown) prior to tumor inoculation (*16*). Also, *ex vivo* immunohistochemical staining of explanted tumors showed high CD20 expression with 100 % positive cells in all slides (Fig. 2A).

Apoptosis and proliferation are further factors that can influence tracer distribution and, thus, were here investigated (Fig. 2A). Immunohistochemical analysis of activated caspase 3 clearly revealed absence of large apoptotic areas, with less than 5 % positively stained cells for total caspase 3. Tumor viability was further confirmed by hematoxylin and eosin (H&E) staining of SUDHL-4 xenografts with a size of 800 mm^3 (Fig. 2B). Notably, according to the Mib1 marker a significantly higher proliferation rate was seen for the Granta xenografts ($p = 0.01$) (Fig. 2C).

Finally, both xenografts showed a homogeneously distributed vasculature with CD31-stained vessels in the tumor center as well as in the periphery (Fig. 2A). However, quantification of vessels revealed that vascularization was significantly higher, by a factor around two, in the Granta xenografts (Fig. 2D).

Investigation of vessel architecture, tumor perfusion, microvascular permeability and tissue penetration

Cy5-labeled Fab-PAS_{200} and the *Bandeiraea (Griffonia) simplicifolia* Lectin-I conjugated with the near infrared (NIR) fluorochrome VivoTag-S 750, as a specific vessel marker, were injected i.v. into both NHL xenograft models in order to correlate the distribution pattern of the Fab within the three-dimensional vessel structure via LSFM (Fig. 3A). Lectin staining revealed well vascularization across the entire xenografts. Notably, in the Granta tumor a heterogeneous distribution of the fluorescently labeled Fab-PAS_{200} was found, similar to the one observed with the radiolabeled Fab using autoradiography. In contrast, SUDHL-4 tumors showed a rim-like distribution pattern, again as seen before using autoradiography. When merging the images obtained for the Fab and the lectin, localization of the Fab only inside the tumor vessels was observed for the SUDHL-4 xenografts whereas the Fab was clearly detected in the perivascular space for the Granta tumors (Fig. 3B). However, not all vessels in the Granta xenografts seemed permeable for Cy5-Fab-PAS_{200} (Supplemental Video 1-5).

Next, non-invasive perfusion experiments using DCE-MRI were performed in CB-17 SCID mice bearing Granta and SUDHL-4 tumor xenografts. The time-dependent concentration curves detected after a bolus injection of the low molecular weight contrast agent Gd-DTPA reveal two major components: first, active perfusion of the tissue based on the arterial input function, which is related to blood flow, and, second, passive diffusion of Gd-DTPA into and out of the extravascular interstitial space, which predominantly depends on vessel permeability and surface area (*17*). A matched single slice from a T2-weighted anatomy scan and a Gd-DTPA T1 map obtained prior to and 15 s after Gd-DTPA injection (Fig. 4A) indicated higher intratumoral Gd-DTPA concentration in Granta compared to SUDHL-4 tumors, in line with the radiotracer distribution experiments. All other organs, including muscles, showed a very similar wash-in pattern independent of the xenograft model. While both tumor models displayed high inter-individual differences, the Granta tumors revealed consistently higher wash-in pattern of Gd-DTPA concentration-time curves compared to the SUDHL-4 tumors (Fig. 4B). Consequently, tumor-to-muscle

ratios of calculated area under the curve values revealed significantly lower perfusion of SUDHL-4 xenografts (Supplemental Fig. 1).

Tumor vessel permeability was further analyzed using the fluorescent perfusion dye H33342, which intercalates into cell nuclei adjacent to permeable blood vessels. For simultaneous detection two consecutive cryo-sections of animals treated with the radiolabeled Fab-ABD or Fab-PAS_{200} and H33342 were analyzed via autoradiography and immunofluorescence, respectively (Fig. 5A). A pronounced heterogeneous distribution of H33324 was observed, but no correlation between the distribution of the Fab and the one of H33342 (Fig. 5B).

Interestingly, comparison of H33342 penetration into the surrounding tumor tissue revealed different patterns: a broad uniform spreading of the perfusion dye was detected in the Granta xenografts, whereas in the SUDHL-4 xenografts merely cells in close proximity to the tumor vessel were stained by H33342 (Fig. 5A). In order to quantify H33342 tissue penetration, image analysis via distance maps was applied and the H33342 intensity was calculated inside tumor vessels as well as in the surrounding tumor tissue. Almost constant H33342 intensity was detected across the Granta xenografts within a distance of 200 µm from a tumor vessel, whereas SUDHL-4 xenografts revealed a rapid decline in dye intensity with increasing distance from a vessel (Fig. 5C).

DISCUSSION

Tumor heterogeneity is one of the main challenges during clinical antibody diagnosis and therapy. Despite prevalent target expression, subgroups of patients do not properly respond to antibody treatment, and the uneven distribution of most antibodies in tumor tissue, including metastases, leaves whole tumor areas or lesions untargeted. Numerous clinical and experimental studies have shown that

Perfusion study of lymphoma xenografts

tumor perfusion has strong impact on both radiotracer uptake and drug delivery. Early detection of changes in tumor permeability and perfusion during treatment would therefore be of great benefit for response prediction. To study the underlying mechanisms for tumor heterogeneity and the role of tumor permeability and perfusion, a well defined preclinical animal model is highly desired. To this end, we characterized two lymphoma xenografts, Granta and SUDHL-4, with apparently similar tumor biology regarding morphology, metabolic activity and CD20 target expression but showing overt differences in perfusion and hemodynamic properties.

Similar autoradiography distribution patterns were found for the small non-targeted radioactive tracer ^{18}F-FDG in both types of xenografts. These result are in accordance with a previous study that investigated SUDHL-4 xenografts using the well established small molecule metabolic tracers ^{18}F-FDG and ^{18}F-FLT (*7*). Likewise, comprehensive investigation of Granta xenografts using CD20-targeting radiolabeled antibody Fab fragments – PAS-Fab and Fab-ABD – applied here revealed strong uptake, similar to an analogous Fab tracer derived from Trastuzumab that was previously investigated in a HER2-positive xenograft model (*8*).

In contrast, almost no specific tumor uptake and a highly unusual rim-like accumulation pattern were observed in SUDHL-4 xenografts for both PASylated and ABD-fused αCD20 Fab versions, and also lower intratumoral Gd-DTPA concentration was detected by DCE-MRI analysis. Furthermore, investigation of tracer localization at a cellular resolution level using LSFM revealed broad transcapillary diffusion of the tracer into the surrounding tissue of Granta tumors, whereas the Fab tracer was mainly located intravascularly in the SUDHL-4 xenografts. H33342 perfusion studies confirmed these results, showing reduced extravasation and tissue penetration of the fluorescent dye in the SUDHL-4 xenografts. Finally, the superior perfusion properties of the Granta xenograft are in line with the immunohistochemical quantification of CD31-positive tumor vessels, which indicated a significantly higher density of tumor vasculature compared to SUDHL-4.

Perfusion study of lymphoma xenografts

The distinct behavior of the CD20-positive SUDHL-4 and Granta xenografts with respect to the various tracers investigated here can be explained in part by their differing biomolecular properties. In comparison to the rapidly excreted small imaging compounds ^{18}F-FDG, Gd-DTPA and H33342 with a molecular size < 1 kDa, both versions of the recombinant αCD20 antibody fragment, Fab-ABD and Fab-PAS_{200}, exhibit much larger apparent molecular sizes of 40 kDa (≥ 100 kDa after association with albumin) and 219 kDa, respectively, and, consequently, much longer plasma half-lives of 29 and 5 h, while having the same antigen affinity (*18*). Low molecular weight compounds usually can rapidly cross the capillary wall, whereas large molecules such as monoclonal antibodies (mAbs) show slower transcapillary and interstitial transport. Therefore, influence of tumor vessel architecture and physiology has a greater impact on macromolecular tracers like antibodies and Fab fragments.

In general, different types of blood vessels are known from the literature. In healthy tissue, a regularly patterned and functional vascularization is found with a normal vessel wall and endothelium. These semipermeable vessels, with a pore size of 5 nm, allow the efflux of both small molecules and proteins up to around 60 kDa but hinder transcapillary transport of larger proteins, in particular antibodies (*19*). For tumors, on the other hand, vessels with a leaky, torturous, dilated and saccular phenotype and a random pattern of interconnections are described, most likely caused by an imbalance of pro- and anti-angiogenic signaling (*20,21*). This perforated phenotype should permit a similar distribution of macromolecular tracers and small molecule reagents outside the tumor vessels. Indeed, in the Granta xenografts we have seen high extravasation for the Fab as well as all three small compounds. Nevertheless, some vessels did not show this leaky phenotype and were impermeable for the αCD20 Fab as observed by LSFM.

Interestingly, the SUDHL-4 xenograft did not match this phenotype, since tumor accumulation of both the Fab-ABD and the small molecules Gd-DTPA and H33342 were clearly reduced. Hence, there seems to occur a second type of distorted tumor vasculature which is characterized by a more closed,

less permeable vasculature. This prevents extravasation of macromolecules and also some small molecules (depending on size, hydrophobicity or charge) whereas low molecular weight metabolites, in particular amino acids and glucose, may still reach the tumor. In fact, such a less permeable vasculature is in accordance with the known low and/or heterogeneous tumor penetration of antibodies and/or drugs previously observed in certain other xenograft models (*22*) and, even more importantly, in patients (*3*).

Interstitial hypertension is another factor in tumor physiology that may play a role for tumor targeting and tissue penetration (*19,22*) which, in principle, could offer another explanation for the low tracer uptake seen here in the SUDHL-4 xenograft tumors. Indeed, high interstitial fluid pressure (IFP) is assumed to prevent efficient tumor penetration of reagents for imaging and therapy in the biomedical literature (*23*). However, while a positive pressure within the tumor tissue would clearly counteract convective molecular transport, it is a misconception that IFP should slow down intratumor molecular diffusion.

IFP is likely caused by local colloid osmotic pressure due to a higher concentration of macromolecules such as polypeptides or proteoglycans in the tumor interstitium. Notably, this phenomenon is somewhat in contradiction with the concept of generally permeable tumor vasculature mentioned above and its consequences for macromolecular accumulation discussed further below. Even in biological systems Newton's law of *actio est reactio* applies, which means that under circumstances of tissue homeostasis the difference in osmotic pressure between capillary lumen and (tumor) interstitium must equal the static pressure between both compartments. In contrast, diffusion is driven by individual concentration differences – i.e., the chemical potential for each molecular species – which is only marginally affected by static pressure (at least at the moderate values prevailing in a living organism).

Apart from that, there are a couple of other aspects which govern efficient tumor targeting, especially for protein-based tracers or drugs (*24*). First, there is the general aspect of vascular

permeability already discussed above. Importantly, most tumors lack lymph drainage, which prevents a convective force that drives permeation of macromolecules through healthy tissues. However, the defective and leaky blood vessels seen in many tumors are considered to cause the so-called enhanced permeability and retention effect. This phenomenon describes the extensive leakage of blood plasma components, in particular large proteins and other macromolecules >40 kDa, into the tumor tissue and their non-specific accumulation there (*25*). While the enhanced permeability and retention effect is in fact assumed to promote tumor targeting by antibodies (as well as liposomes, virus-like particles etc.) it does not guarantee proper distribution within the tumor tissue, beyond the capillary vessel.

On the other hand, the most obvious diffusional barrier within the tumor interstitium is the extracellular matrix – especially in the context of a usually crowded tumor parenchyma – which hampers intratumoral distribution of macromolecules in a size-dependent manner (*26*). While this aspect deserves more detailed investigation, it has become clear that not only glycosaminoglycans but also various collagens form part of the gel-like structure that causes an interstitial transport resistance. Taken together, the situation is complex, and well-defined model systems are clearly needed. The two distinct xenograft tumors characterized in the present study should prove useful to dissect effects of tumor vessel permeability, extracellular matrix composition and, possibly, IFP in dedicated experimental setups.

In the clinical situation, detection and treatment of tumors with a complex and heterogeneous physiology is difficult, and patients often suffer from inefficient diagnostic or therapeutic efficacy. While, for example, the combination of the CD20-specific antibody Rituximab with standard chemotherapy results in higher overall survival and complete response rates in many subtypes of NHL, a significant proportion of patients relapse with incurable disease (*27*). Therefore, assessment of tumor perfusion and permeability in addition to common ^{18}F-FDG-PET staging could considerably improve tumor diagnosis and, eventually, therapy. Indeed, a recently published clinical study showed that perfusion and diffusion

MR imaging correlated with adverse prognosis in immunocompetent patients suffering from primary central nervous system lymphoma (*28*).

Based on our present investigation, the SUDHL-4 xenografts provide a suitable preclinical model to investigate the mechanisms of tumor perfusion and permeability for protein therapeutics and/or tracers, including strategies for tumor vessel normalization or other approaches to improve extravasation and tissue distribution. Several studies have shown that normalization of leaky, abnormal tumor vessels is possible by applying anti-angiogenic therapies such as Bevacizumab (*29*). One study found a decrease in IFP by >70 % and augmented tumor radiation response in two different mouse models bearing human tumor xenografts after anti-VEGF treatment (*30*). During this normalization process, immature vessels were pruned and the integrity and function of the vasculature was improved by enhancing the perivascular cell and basement membrane coverage, eventually resulting in a deeper penetration of molecules into the tumor tissue. Another study demonstrated improvement of specific antibody uptake by targeting the tumor stromal microenvironment with hyaluronidase, thus altering the tumor extracellular matrix (*31*). Consequently, SUDHL-4 xenografts offer a model to study alternative CD20-specific tracers with smaller size and faster diffusion than antibodies, such as Fab fragments, anticalins, affibodies, nanobodies or even peptides.

ACKNOWLEDGEMENTS

This study was supported by ERC Grant MUMI, ERC-2011-ADG_20110310 and by the Deutsche Forschungsgemeinschaft, Collaborative Research Centre SFB 824. The authors wish to thank for Prof. Dr. Buck and Dr. Keller for providing the tumor cell lines SUDHL-4 and Granta.

REFERENCES

1. Spira D, Adam P, Linder C, et al. Perfusion and flow extraction product as potential discriminators in untreated follicular and diffuse large B cell lymphomas using volume perfusion CT with attempt at histopathologic explanation. *Am J Roentgenol.* 2012;198:1239-1246.

2. Scott AM, Wolchok JD, Old LJ. Antibody therapy of cancer. *Nat Rev Cancer.* 2012;12:278-287.

3. Hanaoka K, Hosono M, Tatsumi Y, et al. Heterogeneity of intratumoral ^{111}In-ibritumomab tiuxetan and ^{18}F-FDG distribution in association with therapeutic response in radioimmunotherapy for B-cell non-Hodgkin's lymphoma. *Eur J Nucl Med Mol I.* 2015;5:10.

4. Kalogianni E, Flux GD, Malaroda A. The use of BED and EUD concepts in heterogeneous radioactivity distributions on a multicellular scale for targeted radionuclide therapy. *Cancer Biother Radio.* 2007;22:143-150.

5. Ruan J, Hyjek E, Kermani P, et al. Magnitude of stromal hemangiogenesis correlates with histologic subtype of non-Hodgkin's lymphoma. *Clin Cancer Res.* 2006;12:5622-5631.

6. Gopal AK, Press OW, Wilbur SM, Maloney DG, Pagel JM. Rituximab blocks binding of radiolabeled anti-CD20 antibodies (Ab) but not radiolabeled anti-CD45 Ab. *Blood.* 2008;112:830-835.

7. Graf N, Herrmann K, Numberger B, et al. [^{18}F]FLT is superior to [^{18}F]FDG for predicting early response to antiproliferative treatment in high-grade lymphoma in a dose-dependent manner. *Eur J Nucl Med Mol I.* 2013;40:34-43.

8. Mendler CT, Friedrich L, Laitinen I, et al. High contrast tumor imaging with radio-labeled antibody Fab fragments tailored for optimized pharmacokinetics via PASylation. *MAbs.* 2015;7:96-109.

9. Hamacher K, Coenen HH, Stöcklin G. Efficient stereospecific synthesis of no-carrier-added 2-[^{18}F]-fluoro-2-deoxy-D-glucose using aminopolyether supported nucleophilic substitution. *J Nucl Med.* 1986;27:235-238.

10. Feuchtinger A, Stiehler T, Jütting U, et al. Image analysis of immunohistochemistry is superior to visual scoring as shown for patient outcome of esophageal adenocarcinoma. *Histochem Cell Biol.* 2014;143:1-9.

11. Curti BD, Urba WJ, Alvord WG, et al. Interstitial pressure of subcutaneous nodules in melanoma and lymphoma patients: changes during treatment. *Cancer Res.* 1993;53:2204-2207.

12. Dobosz M. Multispectral fluorescence ultramicroscopy: three-dimensional visualization and automatic quantification of tumor morphology, drug penetration, and antiangiogenic treatment response. *Neoplasia.* 2014;16:1-13.

13. Steingoetter A, Svensson J, Kosanke Y, et al. Reference region-based pharmacokinetic modeling in quantitative dynamic contract-enhanced MRI allows robust treatment monitoring in a rat liver tumor model despite cardiovascular changes. *Magn Reson Med.* 2011;65:229-238.

14. Winkelmann S, Schaeffter T, Koehler T, Eggers H, Doessel O. An optimal radial profile order based on the Golden Ratio for time-resolved MRI. *IEEE T Med Imaging.* 2007;26:68-76.

15. Huber K, Feuchtinger A, Borgmann DM, et al. Novel approach of MALDI drug imaging, immunohistochemistry, and digital image analysis for drug distribution studies in tissues. *Anal Chem.* 2014;86:10568-10575.

16. Meyer zum Büschenfelde C, Feuerstacke Y, Gotze KS, Scholze K, Peschel C. GM1 expression of non-Hodgkin's lymphoma determines susceptibility to rituximab treatment. *Cancer Res.* 2008;68:5414-5422.

17. Gillies RJ, Schornack PA, Secomb TW, Raghunand N. Causes and effects of heterogeneous perfusion in tumors. *Neoplasia.* 1999;1:197-207.

18. Schlapschy M, Binder U, Börger C, et al. PASylation: a biological alternative to PEGylation for extending the plasma half-life of pharmaceutically active proteins. *Protein Eng Des Sel.* 2013;26:489-501.

19. Carmeliet P, Jain RK. Molecular mechanisms and clinical applications of angiogenesis. *Nature.* 2011;473:298-307.

20. Carmeliet P, Jain RK. Principles and mechanisms of vessel normalization for cancer and other angiogenic diseases. *Nat Rev Drug Discov.* 2011;10:417-427.

21. Azzi S, Hebda JK, Gavard J. Vascular permeability and drug delivery in cancers. *Front Oncol.* 2013;3:211.

22. Heine M, Freund B, Nielsen P, et al. High interstitial fluid pressure is associated with low tumour penetration of diagnostic monoclonal antibodies applied for molecular imaging purposes. *PLoS One.* 2012;7:e36258.

23. Heldin CH, Rubin K, Pietras K, Östman A. High interstitial fluid pressure - an obstacle in cancer therapy. *Nat Rev Cancer.* 2004;4:806-813.

24. Al-Abd AM, Aljehani ZK, Gazzaz RW, et al. Pharmacokinetic strategies to improve drug penetration and entrapment within solid tumors. *J Control Release.* 2015;219:269-277.

25. Iyer AK, Khaled G, Fang J, Maeda H. Exploiting the enhanced permeability and retention effect for tumor targeting. *Drug Discov Today.* 2006;11:812-818.

26. Netti PA, Berk DA, Swartz MA, Grodzinsky AJ, Jain RK. Role of extracellular matrix assembly in interstitial transport in solid tumors. *Cancer Res.* 2000;60:2497-2503.

27. Fisher RI. Overview of non-Hodgkin's lymphoma: biology, staging, and treatment. *Semin Oncol.* 2003;30:3-9.

28. Valles FE, Perez-Valles CL, Regalado S, Barajas RF, Rubenstein JL, Cha S. Combined diffusion and perfusion MR imaging as biomarkers of prognosis in immunocompetent patients with primary central nervous system lymphoma. *Am J Neuroradiol.* 2013;34:35-40.

29. Muhsin M, Graham J, Kirkpatrick P. Bevacizumab. *Nat Rev Drug Discov.* 2004;3:995-996.

30. Lee CG, Heijn M, di Tomaso E, et al. Anti-Vascular endothelial growth factor treatment augments tumor radiation response under normoxic or hypoxic conditions. *Cancer Res.* 2000;60:5565-5570.

31. Brekken C, Hjelstuen MH, Bruland ØS, de Lange Davies C. Hyaluronidase-induced periodic modulation of the interstitial fluid pressure increases selective antibody uptake in human osteosarcoma xenografts. *Anticancer Res.* 2000;20:3513-3519.

Perfusion study of lymphoma xenografts

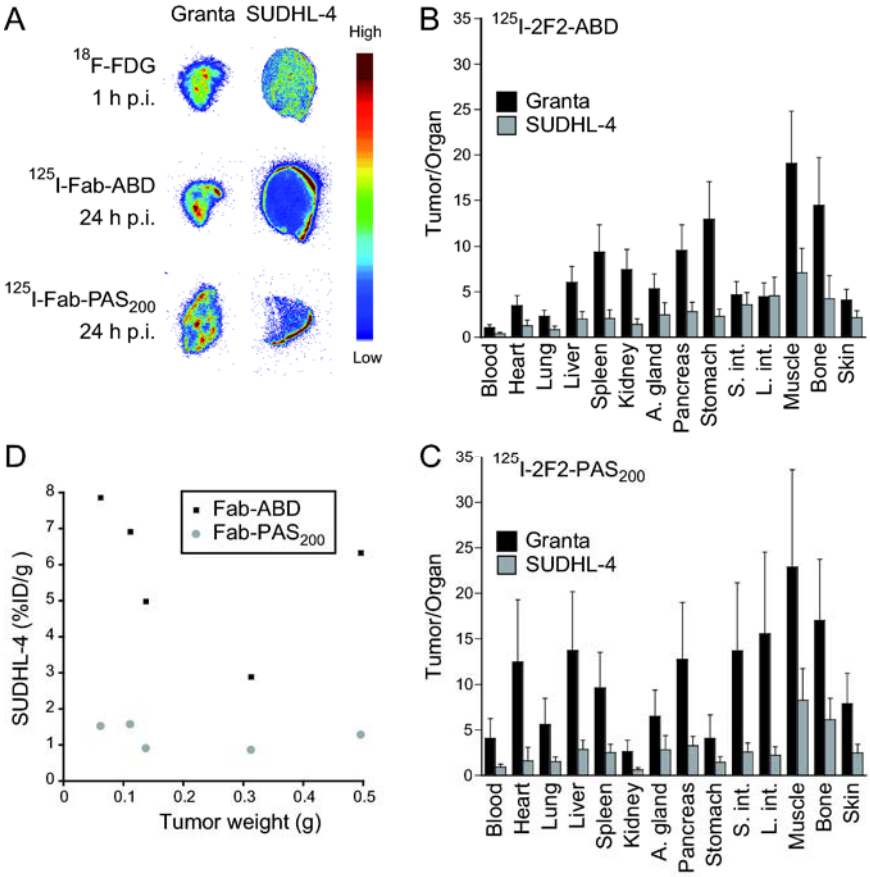

FIGURE 1. Autoradiography and biodistribution studies of Granta and SUDHL-4 tumor xenografts. (A) Autoradiography of tumor xenograft sections from immunocompromised mice was carried out 24 h p.i. of ^{125}I-Fab-ABD or ^{125}I-Fab-PAS$_{200}$ or 1 h p.i. of ^{18}F-FDG. (B,C) Biodistribution studies of Fab-ABD and Fab-PAS$_{200}$ labeled with ^{125}I were conducted 24 h p.i. Tumor-to-organ ratios are plotted for the two αCD20 Fabs (Mean ± SD; n = 5). (D) No strong correlation between tumor uptake and tumor weight was found for SUDHL-4 xenografts 24 h p.i., irrespective of the Fab radiotracer used (Pearson coefficient of -0,32 for Fab-PAS$_{200}$ and -0,36 for Fab-ABD).

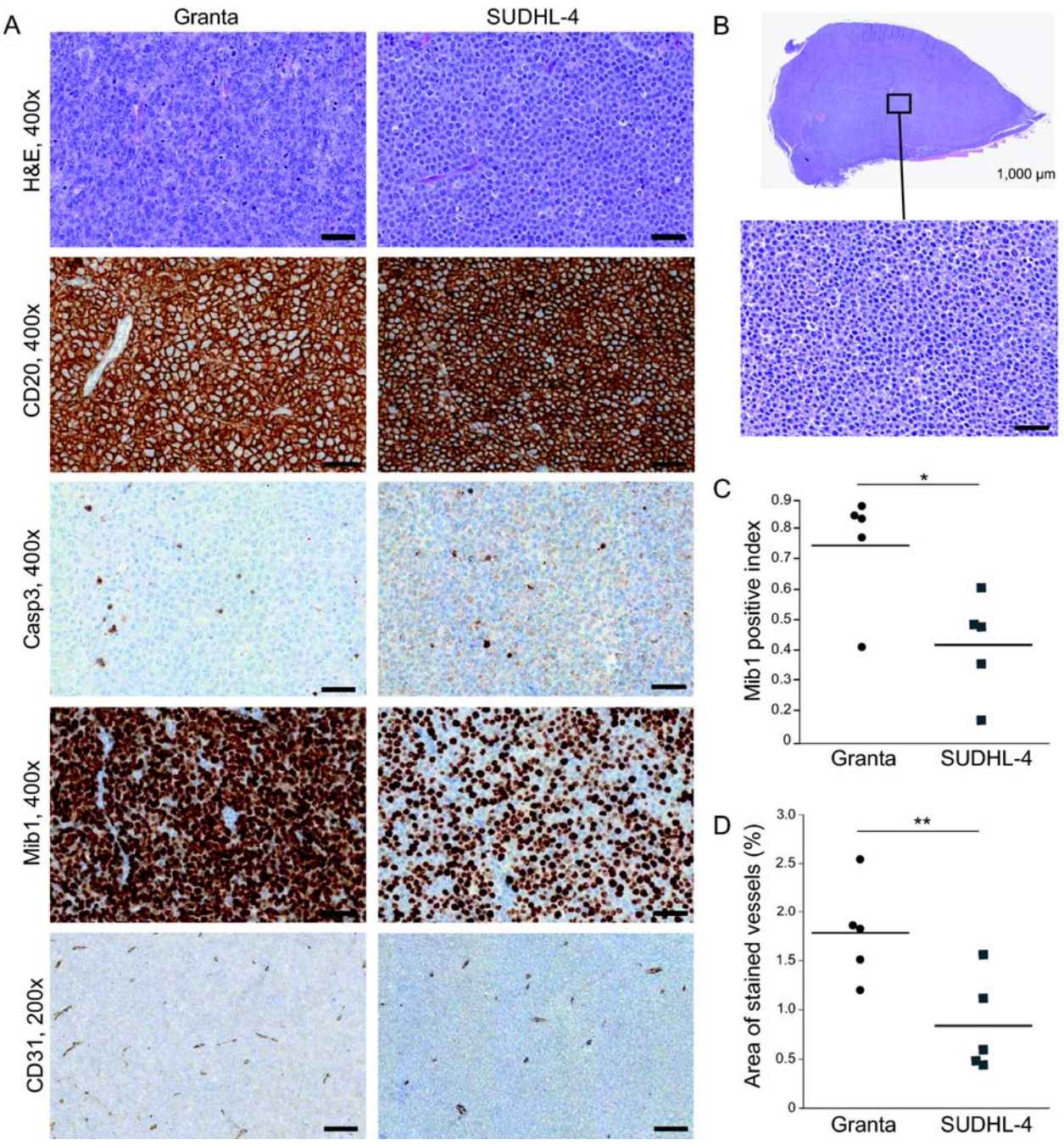

FIGURE 2. Histology and immunohistochemical characterization of Granta and SUDHL-4 tumor xenografts. (A) Explanted lymphoma xenografts were stained with hematoxylin and eosin (H&E) or immunostained for the target antigen CD20, the apoptosis marker caspase 3, the proliferation marker Mib1 and the endothelial marker for tumor vessels CD31 (scale bar 50 µm). (B) H&E staining of an exemplary SUDHL-4 tumor comprising an area of 6x10 mm. (C) Quantification of Mib1 staining reveals

significantly stronger proliferation for Granta than for SUDHL-4 lymphoma xenografts ($p = 0.01$). (D) Quantification of vessel area ($n = 5$) reveals significant higher values for Granta than for SUDHL-4 xenografts ($p < 0.01$).

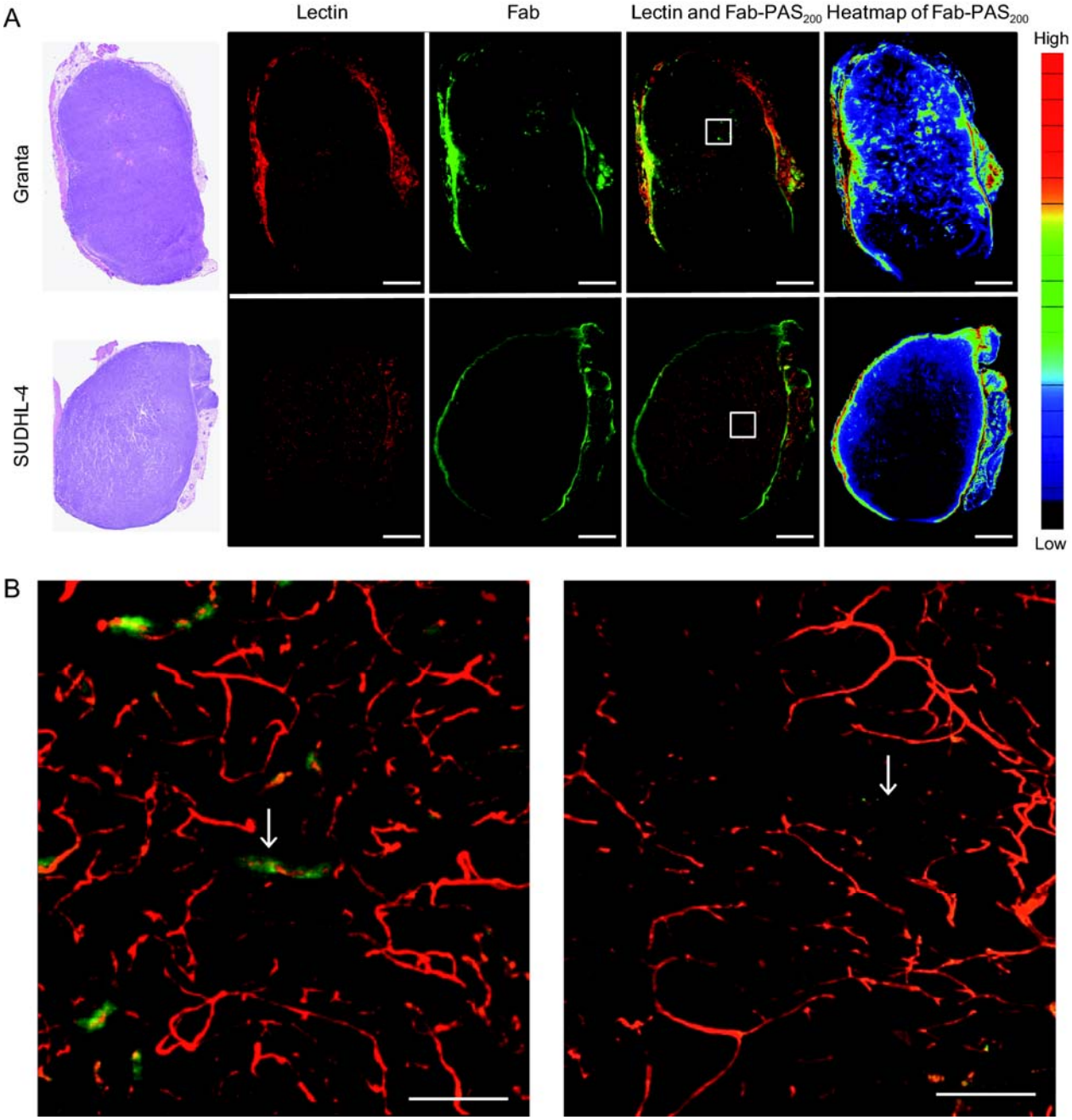

FIGURE 3. Visualization of tumor vessels and αCD20 Cy5-Fab-PAS_{200} distribution in Granta and SUDHL-4 xenografts. Both tumors were stained *in vivo* both with fluorescence-labeled αCD20 Fab-PAS_{200} (24h before sacrification) and with fluorescence-labeled Lectin-I from *Bandeiraea simplicifolia* for vessels (5 min before sacrification) and imaged by LSFM. (A) Both tumors show extensive vascularization (red) throughout the xenograft. For the Granta xenograft a heterogeneous penetration and distribution of the labeled Fab-PAS_{200} (green) across the entire tumor was observed, whereas for the SUDHL-4 xenograft

nearly no Fab-PAS_{200} outside the vessels was detected. The heatmap visualization confirms this different distribution pattern of Granta and SUDHL-4 tumors (scale bar 1500 µm). (B) The different localization of labeled Fab-PAS_{200} (green) in relation to lectin-labeled tumor vessels (red) is clearly visible in the magnified images of a maximum intensity projection of 25 virtual single optical slices. The Granta xenograft shows a perivascular distribution of Fab-PAS_{200}, whereas in the SUDHL-4 xenograft Fab-PAS_{200} is confined to the intravascular space (see arrows).

Perfusion study of lymphoma xenografts

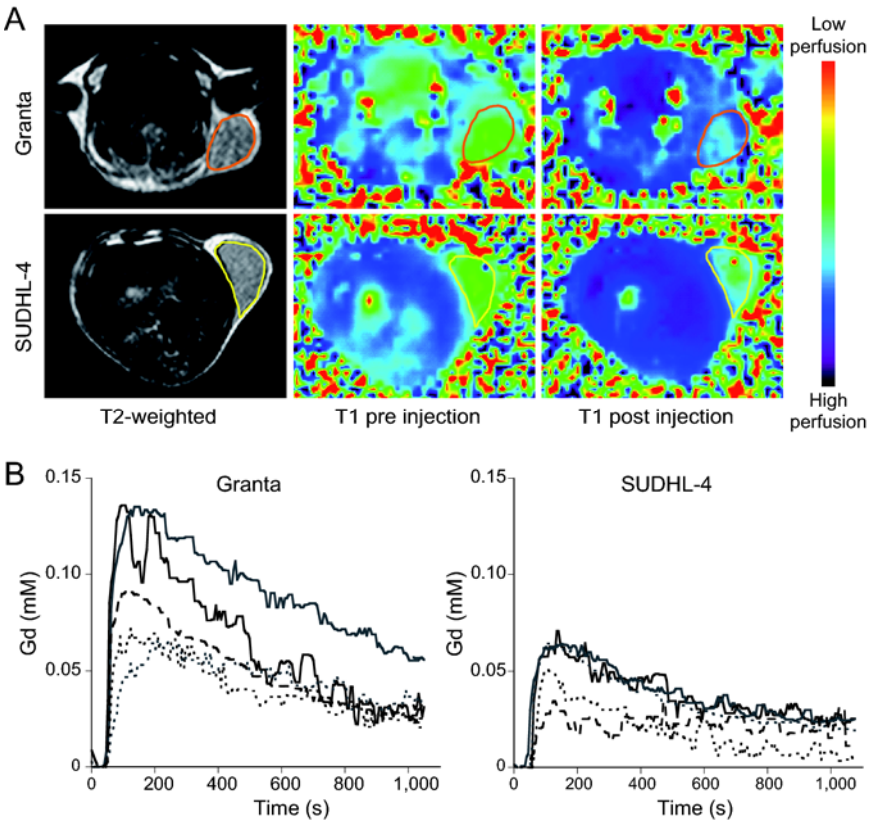

FIGURE 4. DCE-MRI perfusion study of lymphoma xenografts. (A) T2-weighted anatomic images of each one exemplary mouse bearing a Granta or SUDHL-4 tumor and corresponding Gd-DTPA T1 maps with color scale. (B) The Gd concentration curves in individual tumors for Granta xenografts show a higher wash-in pattern compared to SUDHL-4 tumors independent of considerable interindividual variations.

Perfusion study of lymphoma xenografts

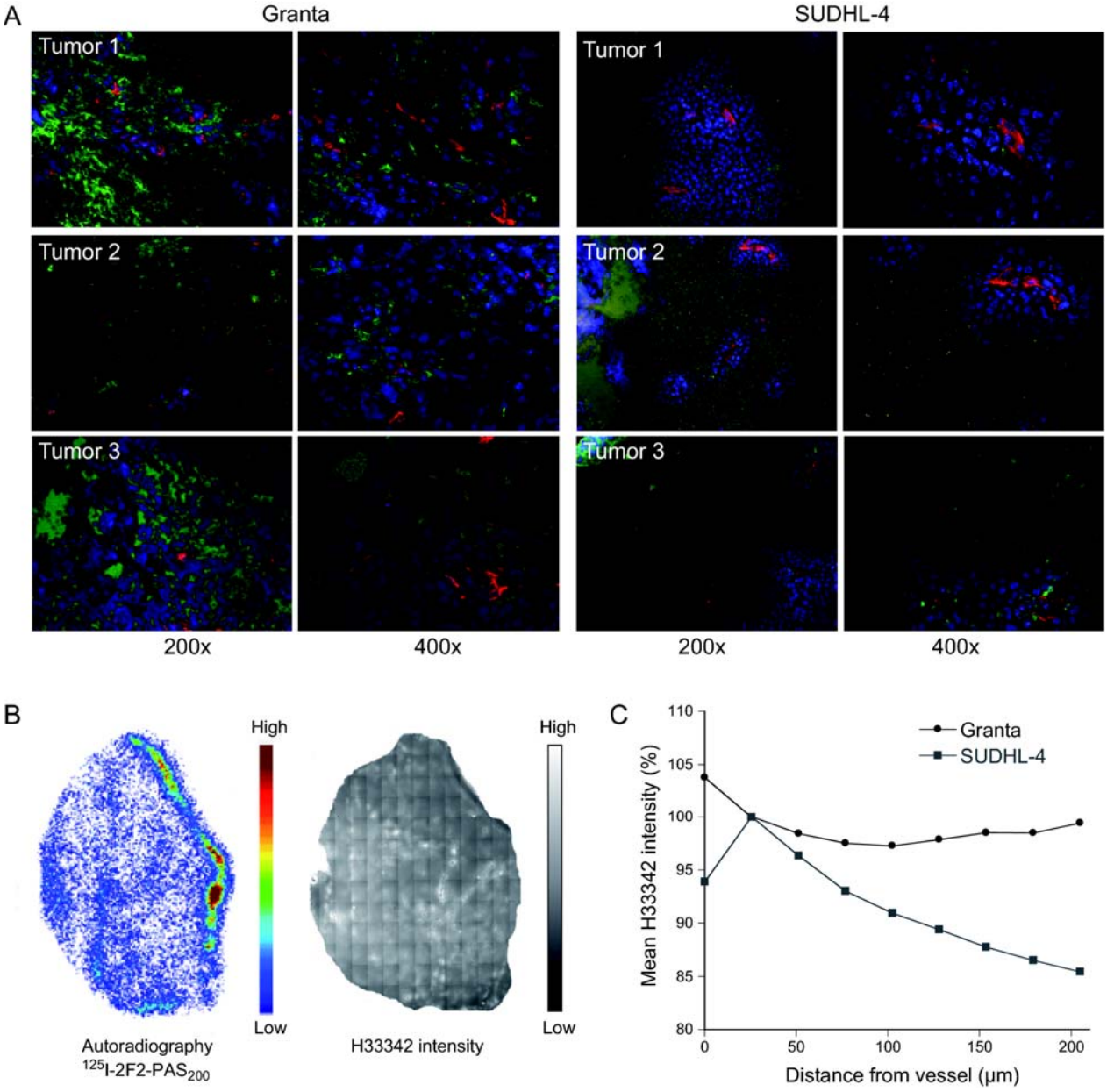

FIGURE 5. Tumor perfusion and tissue penetration of Hoechst33342 in Granta and SUDHL-4 xenografts. (A) The perfusion dye H33342 was injected 24 h after the radioiodinated Fab-ABD or Fab-PAS_{200} and 1 min before the mice were sacrificed. Afterwards, CD20 (green) and CD31 (red) were detected in tumor cryosections using immunofluorescence. H33342 perfusion of three different SUDHL-4 and Granta tumors is represented in blue. (B) Autoradiography and corresponding H33342 intensity is shown for an exemplary SUDHL-4 tumor. (C) Mean H33342 penetration into tumor tissue was quantified using distance maps based on CD31 positive tumor vessels, with a distance equal to zero equivalent to

the tumor vessel lumen. H33342 intensity was normalized with regard to the first distance value (25 µm) after the tumor vessel.